IEEE Access
Multidisciplinary ⋮ Rapid Review ⋮ Open Access Journal

Received 7 December 2023, accepted 19 December 2023, date of publication 28 December 2023,
date of current version 5 January 2024.

Digital Object Identifier 10.1109/ACCESS.2023.3347732

RESEARCH ARTICLE

Investigation of Metal 3-D Printed High-Q Multiband Waveguide Filters Using Spherical Resonators

POVILAS VAITUKAITIS[1], (Graduate Student Member, IEEE), KENNETH NAI[2], AND JIASHENG HONG[1], (Fellow, IEEE)
[1]School of Engineering and Physical Sciences, Heriot-Watt University, EH14 4AS Edinburgh, U.K.
[2]Renishaw PLC, Wotton-under-Edge, GL12 8JR Gloucestershire, U.K.

Corresponding author: Povilas Vaitukaitis (pv30@hw.ac.uk)

This work was supported in part by the Engineering and Physical Sciences Research Council (EPSRC), and in part by Renishaw PLC through the Industrial Cooperative Awards in Science and Technology (ICASE) Studentship (Voucher no. 19000147) under Grant EP/T517471/1.

ABSTRACT This paper proposes a high-Q multiband waveguide filter implementation using spherical resonators and an in-band transmission zeros approach. Three prototype filters in *Ku*-band, one 3rd order triple-band filter with a fundamental TM_{101} mode and two 5th order dual-band filters with TM_{101} and TE_{101} modes, are designed to validate the model. Compared to the previous multiband waveguide filter model using cylindrical resonators, the presented model can realise all expected N transmission zeros between the bands, where N is the filter order, and has a 112% higher simulated Q_u value. Meanwhile, the designed very narrowband dual-band filter using spherical resonators with TE_{101} mode has about 287% higher simulated Q_u value than the same filter would have if using rectangular resonator with TE_{101} mode. For experimental validation, the 3rd order triple-band filter was fabricated using Selective Laser Melting since using traditional milling techniques is not feasible for spherical resonator filters. Monolithic near-net shape fabrication eliminated assembly, improved reliability, and reduced weight. The measured results had a relatively good agreement with the simulations. The measured insertion loss was about 0.54-0.72 dB at the centre frequency of each band, which is a noticeable improvement over the 1.1 dB insertion loss of the previous cylindrical resonator triple-band filter prototype. As there were some deviations between simulated and measured results, the proposed design was inspected in detail, and several improvements for optimising the design for Additive Manufacturing were suggested.

INDEX TERMS Dual-band filter, high-Q, in-band transmission zeros, metal 3-D printing, multiband filter, spherical resonator, triple-band filter, waveguide filter.

I. INTRODUCTION

Multiband waveguide filters are used in communication systems with multiple separated frequency bands to simplify system architecture, reducing weight and cost [1], [2]. There are two primary implementations of multiband filters: combining single-band filters via manifold or circulators or using multimode resonators where each mode corresponds to a specific passband. The former approach provides the best design flexibility [3], [4] but has a large footprint. The latter method has lower design flexibility but significantly reduces footprint [4], [5]. Another, less explored in the literature, method of implementing multiband filters is an in-band transmission zeros (TZs). This approach sits somewhere between the two aforementioned methods. It has better design flexibility but a larger size than multimode resonators and lower design flexibility but a more compact size than the manifold approach [4]. Thus, the in-band TZ approach

The associate editor coordinating the review of this manuscript and approving it for publication was Giorgio Montisci.

presents an excellent middle ground between the two popular implementations.

A high Q-factor is a critical characteristic of waveguide filters. Low insertion loss is a significant property in satellite communications where received power is very low; thus, losses within the receiver may deteriorate the signal quality. Spherical resonators inherently have a higher Q than rectangular and cylindrical resonators for the same resonant frequency, although with a somewhat smaller spurious-free window. With the advent of Additive Manufacturing (AM), it became rather feasible to fabricate complex shapes such as curved surfaces and spherical cavities. Several works report AM of spherical/ellipsoid resonator filters operating at a fundamental TM_{101} mode [6], [7], [8], [9], [10]. A TM_{211} mode was used in [11] and [12] to further increase the Q-factor. Recently, a TE_{101} mode was used to significantly increase the Q-factor of spherical resonator filters, about 1.67 times compared to the fundamental TM_{101} mode at 10 GHz [13], [14]. Besides a very high Q-factor, there are a few other advantages to using TE_{101} mode. Namely, lower dimensional sensitivity since cavities are larger; reduced sensitivity to the surface roughness due to the electric field being concentrated around the centre of the cavity, which minimises the surface currents; and there are additional transmission zeros in both lower and upper stopbands due to higher order modes' coupling.

Spherical resonators have also been used to design dual-band dual-mode filters [15]. The same concept has been extended to elliptical cavities in [16]. Both works used AM to fabricate the prototypes as the geometry is unfit for Computer Numerical Control (CNC) manufacturing. Spherical resonators exhibited higher Q values than rectangular and cylindrical dual-mode counterparts (the Q value in elliptical cavity filters was not reported). However, in both cases, the concept only applies to the dual-band filters. To the best of the author's knowledge, there are no reported multiband spherical resonator filters specifically designed to have high Q value. Therefore, this paper aims to fill the knowledge gap.

This paper presents a high-Q multiband filter implementation using spherical resonators. The proposed model uses an in-band transmission zeros approach like the work presented in [4]. However, there are some key differences:

- Due to the in-line topology of the main coupling path, all expected N TZs between the passbands are realised, where N is the filter order;
- Although there is no cross-coupling, there are TZs in the upper stopband due to higher order modes' coupling;
- Spherical resonators have higher Q value compared to cylindrical resonators for the same resonant frequency; hence lower insertion loss (IL) is expected;
- Even higher Q value can be achieved by utilising higher order modes, such as TE_{101} [13], [14].

This paper is organised as follows. Section II details the resonator analysis, coupling matrix (CM) synthesis for compound resonator topology, filter design, and designed dual-band and triple-band filter prototypes using different spherical resonator modes. Section III presents the experimental results of the triple-band filter prototype, discusses options for further optimisation of the proposed model for AM, and compares filter prototype performance with other state-of-the-art waveguide single- and multiband filters.

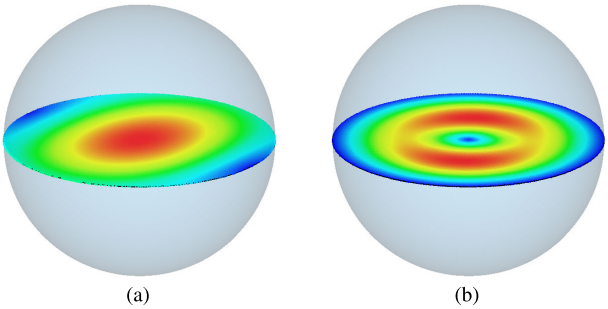

FIGURE 1. Section view of *E*-field distribution of: (a) TM_{101} mode; (b) TE_{101} mode.

II. FILTER DESIGN

A. SPHERICAL RESONATOR ANALYSIS

The spherical cavity supports the propagation of TM_{nmp} and TE_{nmp} modes. The resonant frequency of both types of modes can be calculated as follows [17]:

$$f_{nmp}^{TE} = \frac{u_{np}}{2\pi r\sqrt{\epsilon\mu}} \tag{1a}$$

$$f_{nmp}^{TM} = \frac{u'_{np}}{2\pi r\sqrt{\epsilon\mu}} \tag{1b}$$

where r is the sphere's radius and u_{np} and u'_{np} are the p-th roots of the n-th order spherical Bessel function and its derivative, respectively.

This work uses the fundamental TM_{101} ($u'_{np} = 2.744$) and higher order TE_{101} ($u_{np} = 4.493$) modes. The radii of the spherical cavity resonating at 15 GHz are 8.73 and 14.29 mm for TM_{101} and TE_{101} modes, respectively. Eigenmode simulations using CST Studio Suite confirmed the accuracy of 1, as seen in Table 1.

The *E*-field distribution of both modes is displayed in Fig. 1. TE_{101} mode is concentrated around the cavity centre and, as a result, reduces surface currents on the cavity wall. It should be noted that spherical cavities support several degenerate modes for each mode. However, only one mode is excited if there are no perturbations within the cavity.

Table 1 gives a simulated unloaded quality factor, Q_u, comparison for different resonator types. Spherical cavity has about 73% and 287% higher Q-factor than rectangular and cylindrical cavities operating at 15 GHz frequency for TM_{101} and TE_{101} modes, respectively. Therefore, using a spherical resonator should lead to a reduction of insertion loss in designed filters.

B. COMPOUND RESONATOR TOPOLOGY

Several possible coupling topologies allow to have in-band transmission zeros [1]. Among them, compound resonator

TABLE 1. Comparison of different resonator types.

Type (mode)	Q_u @ 15 GHz	Dimensions (mm)	Spurious modes below/above resonance (GHz)	Volume (mm^3)
Rectangular (TE_{101})	5373	$a = 15.8$ $b = 7.9$ $l = 12.9$	—/21.21	1610
Cylindrical (TM_{010})	5379	$r = 7.65$ $h = 7.15$	—/23.89	1315
Spherical (TM_{101})	9311	$r = 8.73$	—/21.15	2787
Spherical (TE_{101})	20822	$r = 14.29$	12.92/16.61	12223

Bulk aluminium electrical conductivity, 3.56×10^7 S/m, was used in CST eigenmode simulations to calculate the unloaded Q-factor.

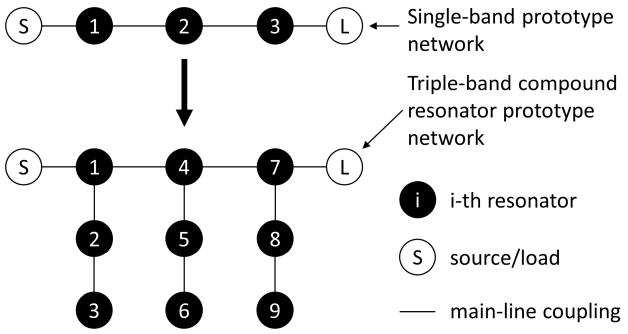

FIGURE 2. Single-band network transformation to the triple-band filter compound resonator network.

topology is the only one that applies to the multiband filters, i.e. where the number of bands is higher than two. This topology allows the realisation of N TZs between each passband and flexible control of centre frequencies and bandwidths. The flexibility of the compound resonator approach was demonstrated in [4], where the reconfigurability of dual-band filtering characteristics was shown with several examples.

The compound resonator coupling topology for a triple-band filter is shown in Fig. 2. The resonance of the shunt resonators controls the realised TZs, i.e. shunt resonators can be considered bandstop resonators. Naturally, reflection poles are controlled by all resonators.

The key to the compound resonator approach is determining the coupling matrix. Brand et al. [18] developed a synthesis method based on reactance transformations. Therefore, for a detailed, in-depth coupling matrix synthesis for compound resonator topology, the reader is directed to [18]. However, for the sake of article cohesion, the main synthesis steps will be briefly introduced. A triple-band filter, which has the exact specification as the manufactured prototype, synthesis will be used as an example to better illustrate the filter design steps.

The compound resonator synthesis is based on a reactance transformation method that develops a frequency mapping function between a single-band prototype network and a multiband compound resonator prototype network. In other words, the function enables each resonator of a single-band

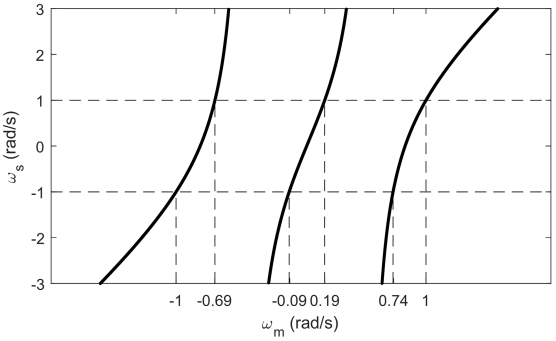

FIGURE 3. Frequency mapping function for a triple-band filter example: band 1 is from 13.1 to 13.5 GHz, band 2 is from 14.3 to 14.7 GHz, and band 3 is from 15.5 to 15.9 GHz.

prototype to be replaced with a compound resonator. The process for a triple-band filter is illustrated in Fig. 2.

The frequency mapping function is composed of two rational polynomials:

$$\omega_s(\omega_{mi}) = \frac{p_{N_b}\omega_{mi}^{N_b} + p_{N_b-1}\omega_{mi}^{N_b-1} + \ldots + p_1\omega_{mi} + p_0}{q_{N_b-1}\omega_{mi}^{N_b-1} + \ldots + q_1\omega_{mi} + 1} = \frac{P(\omega_m)}{Q(\omega_m)} \tag{2}$$

where ω_s is the single-band prototype frequency variable, ω_m is the multiband prototype frequency variable, and N_b is the number of bands. An example of the frequency mapping function for a triple-band filter example is shown in Fig. 3. The multiband filter passband edge frequencies can be normalised using the standard lowpass to bandpass transformation:

$$\omega_m = \frac{1}{\Delta}\left(\frac{\omega}{\omega_0} - \frac{\omega_0}{\omega}\right) \tag{3}$$

where the frequencies in fractional bandwidth, Δ, and centre frequency, ω_0, calculation are the frequencies of the lowest band lower edge and highest band higher edge in the actual frequency domain ω.

As the mapping function alternates between -1 and 1 in ω_s in the -1 to 1 range in ω_m, it passes through $2N_b$ known points. Therefore, a set of $2N_b$ coordinates for the triple-band filter example may be constructed as follows:

$$\begin{aligned}\{\omega_{mi}, \omega_s(\omega_{mi})\} &= \{(-1, 1); (-0.6889, 1); (-0.0949, -1); (0.1895, 1);\\ &\quad (0.7364, -1); (1, 1)\}, \quad i = 1, 2, \ldots, 2N_b\end{aligned} \tag{4}$$

The frequency mapping function in 2 can be rewritten as follows:

$$P(\omega_{mi}) - \omega_s(\omega_{mi})Q(\omega_{mi}) = 0, \quad i = 1, 2, \ldots, 2N_b \tag{5}$$

Therefore, a set of $2N_b$ linear equations may be formed in the matrix form:

$$\mathbf{AX} = \mathbf{B} \tag{6}$$

where $\mathbf{A}$ is a $2N_b \times 2N_b$ square matrix containing $P(\omega_{mi})$ and $-\omega_s(\omega_{mi})Q(\omega_{mi})$, $\mathbf{X}$ is a $2N_b$ column matrix containing the

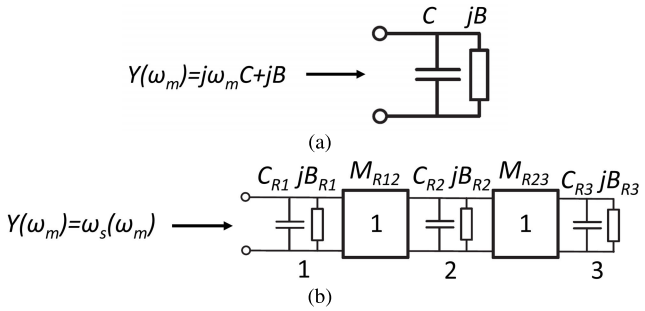

FIGURE 4. Prototype circuits: (a) single-band "lowpass resonator" with frequency-invariant reactance; (b) triple-band compound resonator (adapted from [1]).

unknown coefficients of polynomials $P(\omega_m)$ and $Q(\omega_m)$, and $\mathbf{A}$ is a $2N_b$ column matrix containing the $\omega_s(\omega_{mi})$ values. The full forms of $\mathbf{A}$, $\mathbf{B}$, and $\mathbf{X}$ matrices can be found in [18]. The frequency mapping function is found by solving for $\mathbf{X}$.

The $\mathbf{A}$, $\mathbf{B}$, and $\mathbf{X}$ matrices for the triple-band filter example are as (7), shown at the bottom of the page.

The frequency mapping function can then be constructed:

$$\omega_s(\omega_m) = \frac{-9.9782\omega_m^3 + 0.709\omega_m^2 + 6.692\omega_m - 0.3026}{-4.2862\omega_m^2 + 0.4064\omega_m + 1} \tag{8}$$

The mapping function in 8 is plotted in Fig. 3.

The frequency mapping function may be considered equivalent to an admittance function; therefore, it may be synthesised as a one-port ladder network (compound resonator), which can be used to replace each resonator of any prototype network, as illustrated in Fig. 4 [1]. Classical circuit synthesis techniques may be used to determine the values of capacitors, frequency-invariant reactances (FIRs), and inverters [1]. The values of the components for the triple-band filter example are as follows:

$$\begin{aligned} C_{R1} &= 2.3280 \quad B_{R1} = 0.0553 \quad M_{R12} = 1 \\ C_{R2} &= 0.9873 \quad B_{R2} = -0.0122 \quad M_{R23} = 1 \\ C_{R3} &= 4.3227 \quad B_{R3} = -0.3564 \end{aligned} \tag{9}$$

The single-band prototype network is a simple 3rd order in-line lowpass prototype with 20 dB return loss, which can be synthesised using the classical methods [1]. The coupling matrix for such a network is given as:

$$M_s = \begin{bmatrix} 0 & 1.0825 & 0 & 0 & 0 \\ 1.0825 & 0 & 1.0303 & 0 & 0 \\ 0 & 1.0303 & 0 & 1.0303 & 0 \\ 0 & 0 & 1.0303 & 0 & 1.0825 \\ 0 & 0 & 0 & 1.0825 & 0 \end{bmatrix} \tag{10}$$

Each resonator of the single-band prototype is replaced by the compound resonator, as illustrated in Figs. 2 and 4. All capacitors of both networks at the nodes have to be scaled to unity to obtain the triple-band network coupling matrix. The scaling operations are summarised in two steps, first for the compound resonator network and second for the single-band prototype network. First, scale the compound resonator network components by: $M_{R12} = 1/\sqrt{C_{R1}C_{R2}}$, $M_{R23} = 1/\sqrt{C_{R2}C_{R3}}$, $(B_i + B_{R1})/C_{R1}$ (B_i is the FIR of the single-band prototype network), B_{R2}/C_{R2}, and B_{R3}/C_{R3}. Second, the interresonator couplings in the single-band prototype network coupling matrix have to be divided by C_{R1} and the external couplings by $\sqrt{C_{R1}}$ to scale the capacitors to unity.

The final triple-band network prototype coupling matrix is shown in (11), at the bottom of the next page. In [4], a different multiband synthesis method based on multi-prototype frequency transformation was used to obtain a similar coupling matrix. However, the reactance transformation method [18] is more suitable as it does not involve any optimisation and is easy to implement for many bands and filtering functions with cross-couplings.

C. TRIPLE-BAND FILTER USING TM_{101} MODE

The coupling matrix synthesis was briefly introduced in the previous subsection. The external quality factor, Q_e, and interresonator coupling coefficient, k, graphs must be determined using EM simulations to extract physical filter dimensions from the coupling matrix. The singly loaded resonator group delay and weakly excited coupled resonators methods for extracting external quality factor and

$$\mathbf{A} = \begin{bmatrix} -1 & 1 & -1 & 1 & 1 & -1 \\ -0.3269 & 0.4746 & -0.6889 & 1 & -0.4746 & 0.6889 \\ -0.0009 & 0.0090 & -0.0949 & 1 & 0.0090 & -0.0949 \\ 0.0068 & 0.0359 & 0.1895 & 1 & -0.0359 & -0.1895 \\ 0.3993 & 0.5423 & 0.7364 & 1 & 0.5423 & 0.7364 \\ 1 & 1 & 1 & 1 & -1 & -1 \end{bmatrix},$$

$$\mathbf{B} = \begin{bmatrix} -1 \\ 1 \\ -1 \\ 1 \\ -1 \\ 1 \end{bmatrix}, \quad \mathbf{X} = \begin{bmatrix} -9.9782 \\ 0.7090 \\ 6.6920 \\ -0.3026 \\ -4.2862 \\ 0.4064 \end{bmatrix} \tag{7}$$

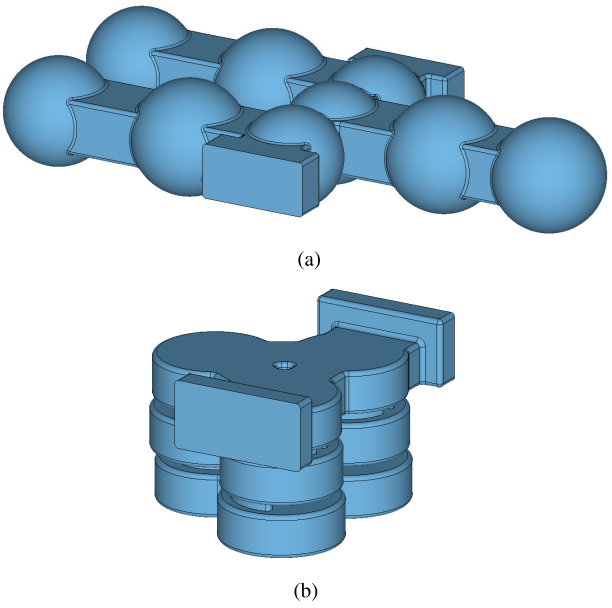

FIGURE 5. 3rd order triple-band filter's 3-D model using: (a) spherical resonators in in-line topology; (b) cylindrical resonators in Olympic topology [4].

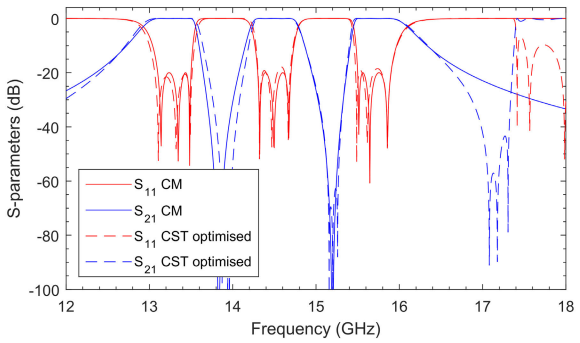

FIGURE 6. Coupling matrix in 11 and optimised simulated lossless, c.f. Table 2, responses of the 3rd order triple-band filter.

interresonator coupling coefficient, respectively, are outlined in [19] and were used here.

The first designed filter is a 3rd order triple-band using spherical resonator fundamental, TM_{101}, mode. It has the exact specification regarding centre frequencies

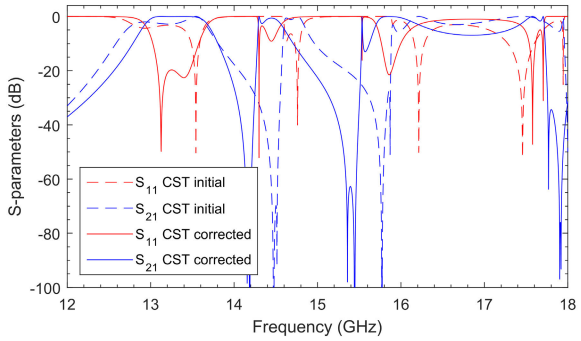

FIGURE 7. Initial and corrected, c.f. Table 2, simulated lossless frequency response of 3rd order triple-band filter.

(13.3/14.5/15.7 GHz) and bandwidths (400 MHz for all channels) as the one presented in [4] for easier comparison. The coupling matrix of this filter is shown in 11. Unless otherwise stated, all simulated results were obtained using bulk aluminium conductivity, 3.56×10^7 S/m.

Fig. 5a shows the filter's 3-D model, and Table 2 summarises the filter's physical dimensions. The irises and resonators are defined according to the coupling topology shown in Fig. 2. The iris thickness, t_{iris}, is defined as the distance between adjacent resonators or port and resonator. a_{iris} is the iris width, and r_{res} is the resonator radius. The height of all irises was set to 7.9 mm. The ports are standard WR62 size. Also, the filter is symmetrical. For simplicity's sake, the dimensions defined in Table 2 are of non-blended filter, i.e. none of the edges are blended. Hence, there is a minor difference in simulated responses between the non-blended filter and the manufactured filter prototype, which had all edges blended.

Coupling matrix and optimised filter response are shown in Fig. 6. The agreement between the two curves is good. Fig. 7 shows the initial and corrected filter responses. The initial dimensions are obtained directly from the coupling matrix via Q_e and k graphs. However, two factors influence the accuracy of physical dimension extraction.

The first is that the coupling matrix method is based on frequency-independent lumped elements; hence, the accuracy of extracting physical dimensions deteriorates as

$$\begin{bmatrix}
0 & 0.7095 & 0 & 0 & 0 & 0 & 0 & 0 & 0 & 0 & 0 \\
0.7095 & 0.0238 & 0.6596 & 0 & 0.4426 & 0 & 0 & 0 & 0 & 0 & 0 \\
0 & 0.6596 & -0.0124 & 0.4841 & 0 & 0 & 0 & 0 & 0 & 0 & 0 \\
0 & 0 & 0.4841 & -0.0824 & 0 & 0 & 0 & 0 & 0 & 0 & 0 \\
0 & 0.4426 & 0 & 0 & 0.0238 & 0.6596 & 0 & 0.4426 & 0 & 0 & 0 \\
0 & 0 & 0 & 0 & 0.6596 & -0.0124 & 0.4841 & 0 & 0 & 0 & 0 \\
0 & 0 & 0 & 0 & 0 & 0.4841 & -0.0824 & 0 & 0 & 0 & 0 \\
0 & 0 & 0 & 0 & 0.4426 & 0 & 0 & 0.0238 & 0.6596 & 0 & 0.7095 \\
0 & 0 & 0 & 0 & 0 & 0 & 0 & 0.6596 & -0.0124 & 0.4841 & 0 \\
0 & 0 & 0 & 0 & 0 & 0 & 0 & 0 & 0.4841 & -0.0824 & 0 \\
0 & 0 & 0 & 0 & 0 & 0 & 0 & 0.7095 & 0 & 0 & 0
\end{bmatrix} \tag{11}$$

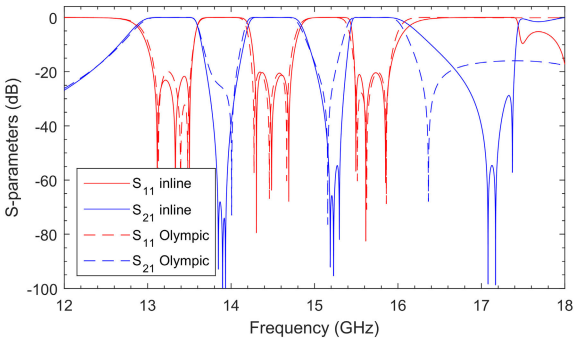

FIGURE 8. Simulated lossless frequency response comparison of 3rd order triple-band in-line filter and Olympic topology 3rd order triple-band filter presented in [4].

the fractional bandwidth (FBW) increases beyond 10% FBW. The FBW of the triple-band filter is 19.4%. The second and far more influential is that Q_e and k graphs are obtained using a simple setup in simulations where resonators are only coupled to the port or each other and the ports. Whereas in the filter, c.f. Fig. 5a, each resonator is coupled to a different number of irises/resonators. Therefore, a manual dimension correction is necessary to obtain a reasonable response for optimisation to account for additional loading or lack of loading. In this case, only some resonators needed a slight correction, c.f. Table 2, to move the bands into the required position as shown in Fig. 7. It should be noted that due to the nature of global EM optimisation, it is not guaranteed to converge. Therefore, optimisation goals and variable range must be appropriately selected, and even then, multiple rounds of optimisation may be required to find the optimal solution.

The middle branch of the filter, c.f. Fig. 5a, was moved to the opposite side to remove design constraints between the resonators of adjacent branches. Also, since overall FBW is large, 19.40%, the physical coupling is strong too. That means using spacing between resonators as a variable is necessary to obtain sufficient coupling strength. Hence, the main-line resonators intersect. Using the irises' thickness as an optimisation variable also increases the degrees of freedom, which makes optimisation easier. In a filter where overall FBW is small, all branches can be on the same side, thus reducing weight as there are more common walls. Such a case will be demonstrated in the following subsection.

The spherical triple-band filter in in-line configuration and cylindrical triple-band filter in Olympic configuration [4] responses are shown in Fig. 8. The in-line configuration allows to realise all N transmission zeros between passbands. Therefore, the rejection between passbands is higher. Without cross-coupling, which is possible in Olympic topology (see Fig. 5b), there is no TZ in the upper stopband; thus, the selectivity of the upper band is lower. However, there are three TZs further in the upper stopband resulting from higher order modes' coupling. Although it is impossible to control them, they can still benefit rejection response in the stopband.

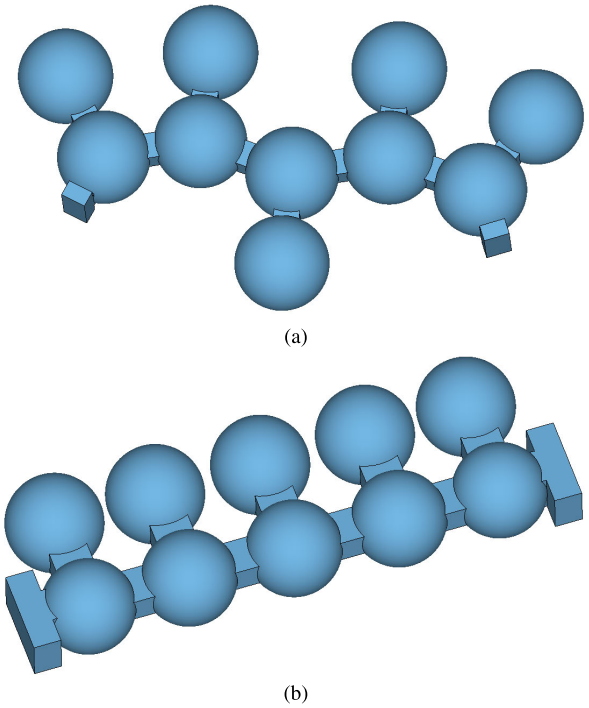

FIGURE 9. 5th order dual-band filter's 3-D model using: (a) TE_{101} mode; (b) TM_{101} mode.

Table 1 gives a comparison of the Q-factor for different resonator types. Spherical resonator with the fundamental mode has about 73% higher Q-factor than rectangular and cylindrical resonators at 15 GHz working frequency. However, in [4], cylindrical resonators with height, $h = 5$ mm, were used, which resulted in a Q_u of 4402. The lower height of the cylindrical resonators was used since the first spurious is not from higher order modes of the cylindrical resonator but from vertical coupling iris. Hence, compared to [4], the theoretical Q_u is about 112% larger when using spherical resonators with fundamental mode. However, a higher Q-factor comes at the cost of a somewhat smaller spurious-free window.

D. DUAL-BAND FILTER USING TE_{101} MODE

The second designed filter is a 5th order dual-band using spherical resonator TE_{101} mode to enhance the Q-factor further. The passbands are centred around 14.575/14.85 GHz with 100 MHz bandwidth for both channels, i.e. with an FBW of less than 1%. To compare the performance of TE_{101} and TM_{101} modes, a third filter was designed using the exact specification but with a TM_{101} mode. The electric fields of both modes, and 3-D models and frequency responses of both filters are shown in Figs. 1, 9, and 10, respectively.

Filter with TE_{101} has TZs below and above the passbands that can enhance the stopband rejection and filter selectivity. These transmission zeros caused by the spurious modes' coupling can be controlled to some degree by varying the excitation angle of each resonator, i.e. coupling aperture angular position w.r.t. each resonator. This was demonstrated

TABLE 2. Main parameters of 3rd order triple-band filter design example.

Parameter	Value (mm)			Parameter	Value (mm)			Parameter	Value (mm)		
	Initial	Corrected	Optimised		Initial	Corrected	Optimised		Initial	Corrected	Optimised
a_{irisS1}	10.85	10.85	9.9899	t_{irisS1}	0	0	-1.1513	r_{res1}	8.51	7.5	7.0367
a_{iris12}	10.43	10.43	10.7708	t_{iris12}	0	0	1.4566	r_{res2}	7.49	7.75	8.0965
a_{iris23}	9.65	9.65	10.1674	t_{iris23}	0	0	3.8358	r_{res3}	7.82	8.25	7.7953
a_{iris14}	9.48	9.48	7.8530	t_{iris14}	0	0	-2.8359	r_{res4}	7.96	7.96	7.3154
a_{iris45}	10.43	10.43	11.0458	t_{iris45}	0	0	2.3046	r_{res5}	7.49	7.75	8.0520
a_{iris56}	9.65	9.65	9.7750	t_{iris56}	0	0	0.6785	r_{res6}	7.82	8.25	7.9517

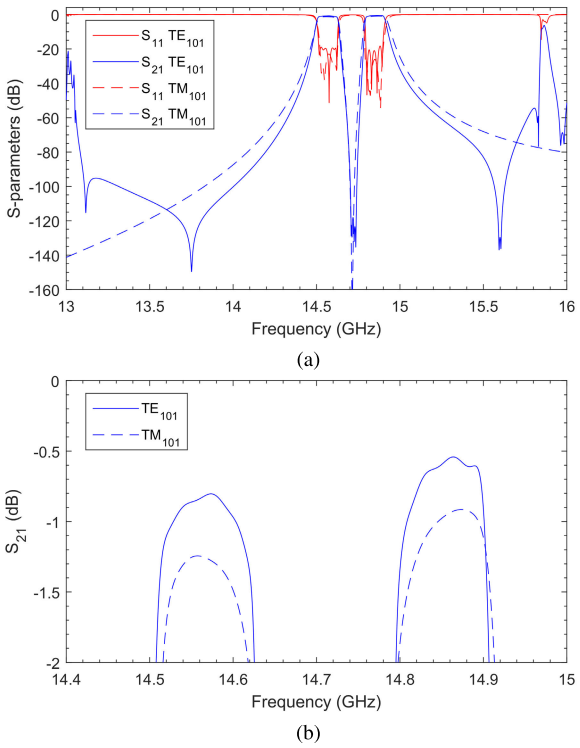

FIGURE 10. Comparison of 5th order dual-band filters using TM_{101} and TE_{101} modes: (a) wideband response; (b) in-band S_{21} response. 20 $\mu\Omega \cdot$ cm electrical resistivity was used in simulations.

in [14]. However, the filter with TM_{101} has a much wider spurious-free window, with the first spurious resonance appearing above 19 GHz.

The simulated frequency responses shown in Fig. 10 were obtained using the effective metal resistivity of 20 $\mu\Omega \cdot$ cm that accounts for the bulk metal resistivity and surface roughness. This value was previously reported to be accurate for 3-D printed and post-processed (shot-peening) devices using AlSi10Mg material [20], [21]. Fig. 10b shows an insertion loss comparison between both designed filters. While IL is also affected by the return loss (RL), and both filters have slightly different RL, the difference between expected IL in 3-D printed prototypes is evident.

As shown in Table 1, the theoretical Q_u of the spherical resonator working in TE_{101} mode is about 124% and 287%

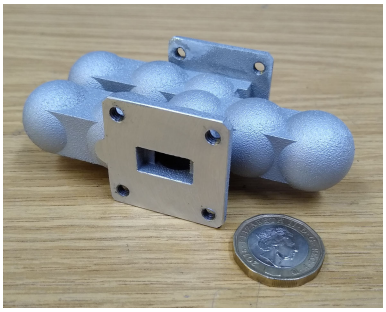

FIGURE 11. Photo of the 3rd order triple-band filter prototype fabricated using SLM (Renishaw RenAM 500Q machine).

higher compared to the spherical resonator with fundamental TM_{101} mode and rectangular resonator, respectively. However, the spurious resonances appear relatively close below and above the propagating mode, limiting the available bandwidth for multiband operation. Furthermore, as the cavity is larger and TE_{101} mode's maximum electric field is concentrated around the middle of the cavity, refer to Fig. 1b, the realisable physical coupling is lower; hence, the achievable bandwidth of each band is also limited.

Therefore, these filters that use higher order modes are only suited for very narrowband applications. However, as is well known, insertion loss degrades as the bandwidth decreases; thus, a high Q value is crucial for very narrowband designs.

III. EXPERIMENTAL RESULTS AND DISCUSSION

To experimentally validate the proposed model, a 3rd order triple-band filter using spherical resonators with fundamental mode was manufactured using Selective Laser Melting. The prototype was fabricated using AlSi10Mg powder. The printed triple-band filter prototype is shown in Fig. 11.

A. MEASURED RESULTS

The prototype was tested as-built, i.e. no surface post-processing was applied. The measured results of the manufactured prototype are shown in Fig. 12. The agreement between the measured results and simulation is primarily good, particularly in the second passband. Some discrepancies in the first passband and in and around the third passband will be discussed in detail in the following subsection.

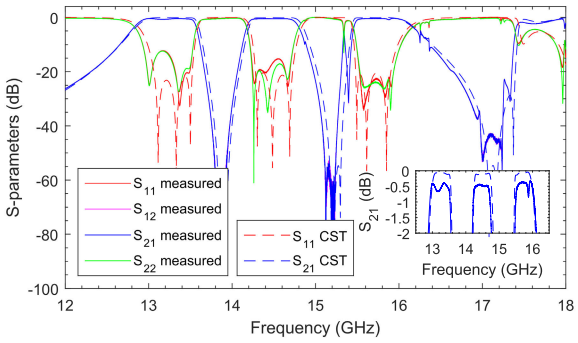

FIGURE 12. 3rd order triple-band filter prototype's measured response (inset: insertion loss).

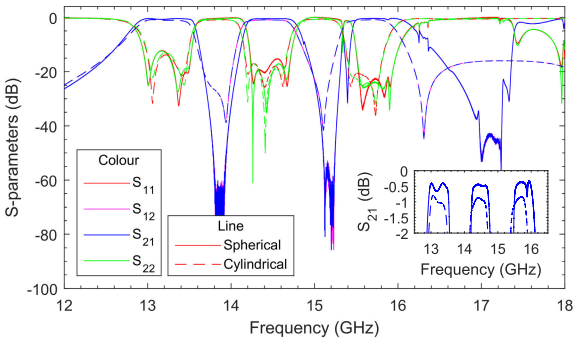

FIGURE 13. Measured frequency response comparison of 3rd order triple-band in-line filter and Olympic topology 3rd order triple-band filter presented in [4] (inset: insertion loss).

The measurement setup was identical to the one in [22]; thus, the measured results include losses from two coaxial to waveguide adapters. The simulated and measured insertion loss is about 0.54-0.72 dB at the centre frequency of each band. The measured in-band return loss is lower than 13 dB across all bands.

Fig. 13 compares measured results with previously reported cylindrical triple-band filter. The results are mostly similar except for the third passband. However, the spherical resonator filter exhibits two superior properties: the full realisation of transmission zeros between the passbands and lower insertion loss due to high-Q resonators.

Since the prototype was not post-processed, it would be valuable to approximately evaluate the effective resistivity of unpolished AlSi10Mg. The middle passband has the best performance in terms of RL, which is only slightly lower than simulated RL. Therefore, it was used to compare the transmission coefficient, as shown in Fig. 14. The results suggest that unpolished AlSi10Mg has an effective resistivity of about 80 $\mu\Omega$·cm. Surface post-processing could reduce resistivity to around 20 $\mu\Omega$·cm, thus improving insertion loss from 0.5 dB to 0.2 dB at centre frequency.

B. TOWARDS AM OPTIMISED DESIGN

There are two main discrepancies between the simulated and measured results. The first is noticeably lower RL in the first passband, and the second is the spikes in response around the third passband.

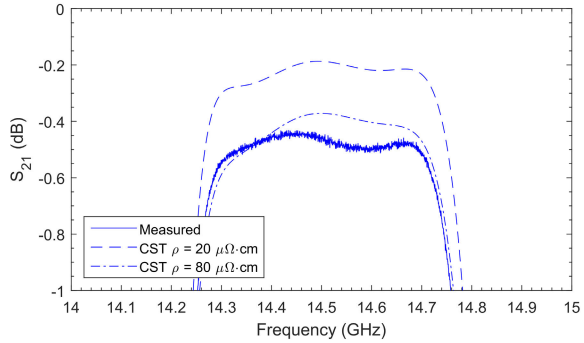

FIGURE 14. Middle band's measured transmission coefficient comparison with simulated response using different effective resistivity values. A frequency shift of 30 MHz was applied to the measured curve for easier comparison.

A larger coupling value between the main-line resonators causes the first deviation. Section view of the spherical resonator triple-band filter prototype CAD model is shown in Fig. 15a. Since main-line resonators overlapped, the iris created is circular, and the formed ridge is very narrow. The ridge was blended with a 0.5 mm radius to remove the sharp edge. However, the rectangular coupling iris from the middle main-line resonator to the first side branch resonator intersects with the circular iris between the main-line resonator, thus creating a sharp edge. Additionally, as seen in Fig. 15a, the rectangular coupling iris between the main-line resonators was not removed, creating unnecessary fine features at the corners of the circular coupling iris. Therefore, to improve 3-D printing quality and measured performance, a larger blend radius should be used for circular iris between main-line resonators, and rectangular coupling iris between main-line resonators should be removed unless the required coupling is small and resonators only slightly intersect or do not intersect at all.

As seen in Fig. 13, the first passband's measured performance is very similar. In the cylindrical model, the larger coupling between main-line resonators is caused by the smaller metal post between three top-row resonators, c.f. Fig. 15b, in the fabricated prototype. That post should also be blended using a larger radius to improve the printing quality and measured performance.

The second deviation, and to some degree the first, is caused by monolithically 3-D printing spherical cavities, resulting in sagging of the top surface because of the shallow print angle at the top. The CAD model positioned in a printing direction in 3-D printing build preparation software QuantAM is shown in Fig. 16. The software recommends supports inside the filter to support the overhanging top surface. Since there would be no way of removing supports inside, the prototypes were printed without them. One of the two manufactured prototypes was cut in half to inspect the quality of the inside surface. The two halves of the cut prototype are shown in Fig. 17. There is a noticeable difference in printing quality between the two halves. The sagging of the top surface of the spherical cavities is evident.

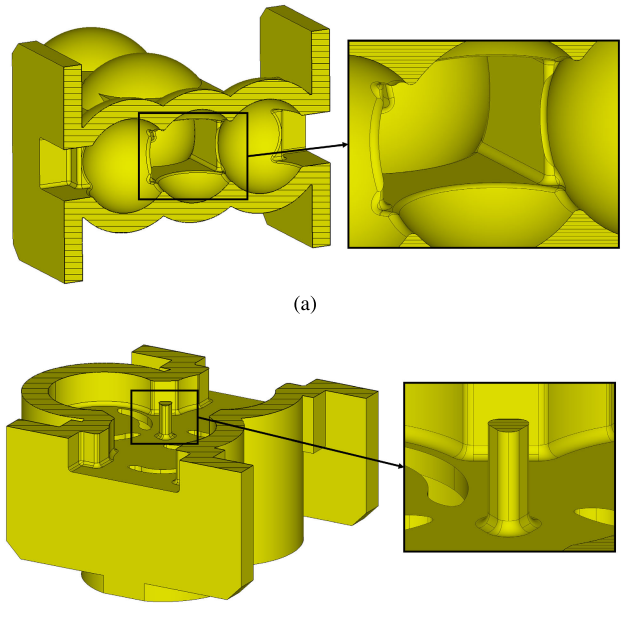

FIGURE 15. CAD model section views of: (a) spherical resonator triple-band filter; (b) cylindrical resonator triple-band filter [4].

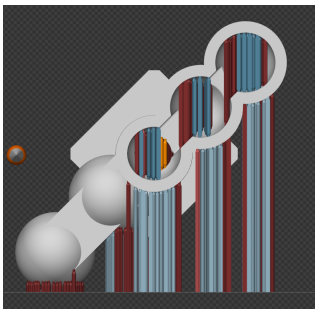

FIGURE 16. Side view of the cross-section of the prototype's CAD model in 3-D printing build preparation software QuantAM [23].

Furthermore, the top half has a downskin surface which is much rougher than the bottom half's upskin surface. Also, the downskin surface roughness was exacerbated by the sagging. Therefore, surface polishing should reduce deviations between measured and simulated results.

There are several ways to improve the manufacturing quality of the presented model. One is to print the filter in two parts, thus avoiding overhangs and downskin surfaces but requiring assembly. Printing in two parts would also allow copper/silver plating to be applied, significantly improving surface finish and electrical conductivity. Another is using micro SLM with a thinner layer thickness, 7 μm [24], compared to 25-30 μm in SLM. Thinner layers would improve the surface finish and reduce the size of each layer's overhang, thus potentially reducing sagging at the top of the spherical cavities. Although, thinner layers would not entirely eliminate overhangs and sagging. Furthermore, micro SLM has a smaller build volume and is a slower process, making it more expensive. Yet another way would

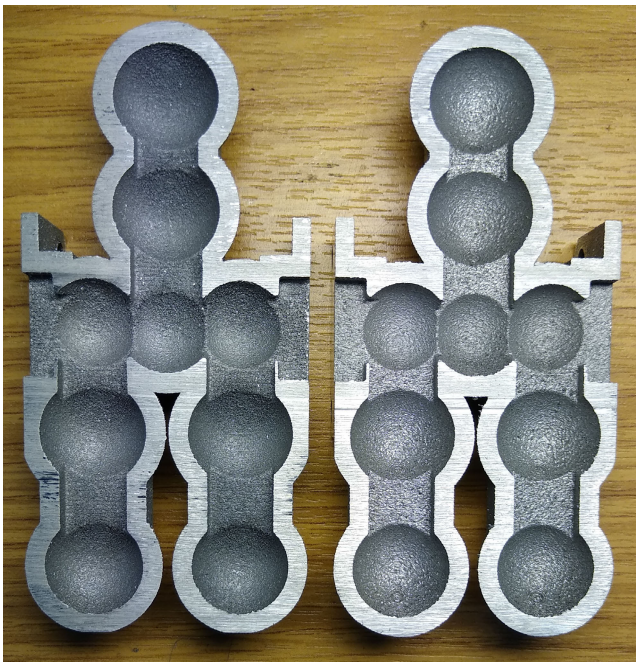

FIGURE 17. Photo of the prototype's top (left) and bottom (right) halves.

be to measure the initial prototype and compensate for the dimensional tolerance in the build preparation software. Adequate repeatability of SLM was proven in previous works [20], [22], [25]; therefore, it should be possible to eliminate systematic dimensional tolerance errors.

Additionally, surface post-processing should be applied whether filters are printed in one or two parts to reduce surface roughness and improve insertion loss [6]. While copper-printed parts can be electro-polished using the usual process, AlSi10Mg parts have a high silicon content making them unsuitable for electro-polishing [22]. Recently, an electrochemical polishing was proposed that reduced surface roughness (Sa) by 87.7%, from 14.90 μm to 1.84 μm [26]. The effects of such electrochemical polishing could be investigated in the future regarding the insertion loss reduction.

C. COMPARISON WITH STATE-OF-THE-ART

Table 3 summarises a quantitative comparison of recently reported state-of-the-art single- and multiband filters. A variety of filters with different specifications, manufacturing technologies, materials, and post-processing techniques have been selected.

The triple-band prototype has a comparable performance in terms of IL and RL. Especially considering that no post-processing was applied. As previously discussed, c.f. Fig. 14, surface polishing would increase the IL to about 0.2 dB. At this point, the performance could be similar to those filters manufactured with CNC. Additionally, AM has the advantage of monolithic near-net shape fabrication, eliminating assembly, improving reliability, and reducing weight.

TABLE 3. Comparison with previously reported state-of-the-art single- and multiband filters.

Ref.	f_0 (GHz)	FBW (%)	N	IL (dB)	RL (dB)	Q_u	Manufacturing technology	Material	Post-processing	Assembly
[3]	11/12/13	1.82/2.5/3.08	6	0.21-0.49	>19.5	N/A	CNC	Aluminium	Silver plating	Yes
[9]	10	5	5	0.2-0.3	>15	3840-5195	SLM	Aluminium alloy	Vibration grinding surface polishing	No
[11]	31	2.84	4	1.53	>13.6	7393	SLM	AlSi10Mg	Chemical surface polishing	No
[15]	12/12.49	1/1.92	2	0.45-0.6	>20	12379	SLS	PA12 (nylon)	Copper plating	No
[22]	14.23	10.54	4	0.67-0.97	>12	1728-1937	SLM	Copper powder	Electro-polishing	No
[27]	10/15	2/2	3	0.28-0.55	>8	2478/4961	CNC	Copper	Silver plating	Yes
T.W.	13.3/14.5/15.7	3/2.76/2.56	3	0.54-0.72	>13	9311	SLM	AlSi10Mg	None	No

T.W. – this work; f_0 – centre frequency; FBW – fractional bandwidth; N – filter order; IL – insertion loss; RL – return loss; Q_u – simulated unloaded quality factor of a single resonator; N/A – not available; CNC – computer numerical control; SLS – selective laser sintering; SLM – selective laser melting.

IV. CONCLUSION

This paper proposed a high-Q multiband waveguide filter implementation based on the in-band transmission zeros approach. Two prototype filters were designed using spherical cavity resonators, one with a fundamental TM_{101} mode and another with a higher order TE_{101} mode. The former prototype filter was metal 3-D printed using Selective Laser Melting. The measured results had a relatively good agreement with simulations. Notably, the prototype exhibited a lower insertion loss compared to the previous work, which is promising for future high-Q multiband filters. Furthermore, several suggestions were proposed to optimise the filter design for Additive Manufacturing and hence improve measured RF performance.

In the future, the same filter model could be post-processed and retested to establish the effect of surface polishing. If the results prove unsatisfactory, the same prototype could be printed in two parts and copper/silver plating could be applied to obtain better surface finish and higher conductivity.

ACKNOWLEDGMENT

The authors would like to thank the staff at Renishaw and the mechanical workshop at Heriot-Watt for their help in manufacturing the prototypes.

REFERENCES

[1] R. J. Cameron, C. M. Kudsia, and R. R. Mansour, *Microwave Filters for Communication Systems: Fundamentals, Design, and Applications*, 2nd ed. Hoboken, NJ, USA: Wiley, 2018.

[2] S. Holme, "Multiple passband filters for satellite applications," in *Proc. 20th AIAA Int. Commun. Satell. Syst. Conf. Exhib.*, May 2002, p. 1993.

[3] J. C. Melgarejo, S. Cogollos, M. Guglielmi, and V. E. Boria, "A new family of multiband waveguide filters based on a folded topology," *IEEE Trans. Microw. Theory Techn.*, vol. 68, no. 7, pp. 2590–2600, Jul. 2020.

[4] P. Vaitukaitis, K. Nai, and J. Hong, "A versatile 3-D printable model for implementing multiband waveguide filters with flexible filtering characteristics," *IEEE Access*, vol. 11, pp. 110051–110059, 2023.

[5] L. Zhu, R. R. Mansour, and M. Yu, "Triple-band cavity bandpass filters," *IEEE Trans. Microw. Theory Techn.*, vol. 66, no. 9, pp. 4057–4069, Sep. 2018.

[6] F. Zhang, S. Gao, J. Li, Y. Yu, C. Guo, S. Li, M. Attallah, X. Shang, Y. Wang, M. J. Lancaster, and J. Xu, "3-D printed slotted spherical resonator bandpass filters with spurious suppression," *IEEE Access*, vol. 7, pp. 128026–128034, 2019.

[7] Y. Li, J. Li, M. Zhang, H. Wang, J. Xu, and S. Xiao, "A monolithic stereolithography 3-D printed Ka-band spherical resonator bandpass filter," in *Proc. IEEE Radio Wireless Symp. (RWS)*, Jan. 2018, pp. 56–59.

[8] X. Wen, C. Guo, X. Shang, Y. Yu, M. Shu, Q. Yang, S. Li, M. M. Attallah, H. Liu, and A. Zhang, "SLM printed waveguide dual-mode filters with reduced sensitivity to fabrication imperfections," *IEEE Microw. Wireless Compon. Lett.*, vol. 31, no. 11, pp. 1195–1198, Nov. 2021.

[9] C. Guo, Y. Yu, S. Li, X. Wen, A. Zhang, Y. Wang, and M. Attallah, "Monolithic 3D printed waveguide filters with wide spurious-free stopbands using dimpled spherical resonators," *IET Microw., Antennas Propag.*, vol. 15, no. 12, pp. 1657–1670, Oct. 2021.

[10] C. Guo, X. Shang, M. J. Lancaster, and J. Xu, "A 3-D printed lightweight X-band waveguide filter based on spherical resonators," *IEEE Microw. Wireless Compon. Lett.*, vol. 25, no. 7, pp. 442–444, Jul. 2015.

[11] F. Zhang, C. Guo, Y. Zhang, Y. Gao, B. Liu, M. Shu, Y. Wang, Y. Dong, M. J. Lancaster, and J. Xu, "A 3-D printed bandpass filter using TM_{211}-mode slotted spherical resonators with enhanced spurious suppression," *IEEE Access*, vol. 8, pp. 213215–213223, 2020.

[12] Y. Zhang, X. Shang, and J. Xu, "Design of WR5 waveguide bandpass filter using oversized spherical resonators," in *Proc. 14th UK Europe-China Workshop Millimetre-Waves Terahertz Technol. (UCMMT)*, Sep. 2021, pp. 1–3.

[13] E. López-Oliver, C. Tomassoni, G. Addamo, F. Calignano, M. Lumia, O. Peverini, and G. Virone, "Very high Q-factor bandpass filter using additive manufacturing," in *IEEE MTT-S Int. Microw. Symp. Dig.*, Nov. 2021, pp. 243–245.

[14] E. López-Oliver and C. Tomassoni, "Stereolithography additive manufacturing of overmoded spherical filters," in *Proc. Microw. Medit. Symp. (MMS)*, May 2022, pp. 1–4.

[15] Y. Chen, G. Zhang, J. Hong, Z. Sun, J. Yang, W. Tang, and C. Feng, "3-D printed dual-band filter based on spherical dual-mode cavity," *IEEE Microw. Wireless Compon. Lett.*, vol. 31, no. 9, pp. 1047–1050, Sep. 2021.

[16] E. López-Oliver and C. Tomassoni, "Dual-band filters based on dual-mode ellipsoidal cavities," in *IEEE MTT-S Int. Microw. Symp. Dig.*, Jun. 2022, pp. 88–91.

[17] C. A. Balanis, *Advanced Engineering Electromagnetics*, 2nd ed. Hoboken, NJ, USA: Wiley, 2012.

[18] T. G. Brand, P. Meyer, and R. H. Geschke, "Designing multiband coupled-resonator filters using reactance transformations," *Int. J. RF Microw. Comput. Aided Eng.*, vol. 25, no. 1, pp. 81–92, Jan. 2015.

[19] J.-S. Hong, *Microstrip Filters for RF/Microwave Applications*, 2nd ed. Hoboken, NJ, USA: Wiley, 2011.

[20] O. A. Peverini, M. Lumia, F. Calignano, G. Addamo, M. Lorusso, E. P. Ambrosio, D. Manfredi, and G. Virone, "Selective laser melting manufacturing of microwave waveguide devices," *Proc. IEEE*, vol. 105, no. 4, pp. 620–631, Apr. 2017.
[21] G. Addamo, O. A. Peverini, D. Manfredi, F. Calignano, F. Paonessa, G. Virone, R. Tascone, and G. Dassano, "Additive manufacturing of Ka-band dual-polarization waveguide components," *IEEE Trans. Microw. Theory Techn.*, vol. 66, no. 8, pp. 3589–3596, Aug. 2018.
[22] P. Vaitukaitis, K. Nai, J. Rao, M. S. Bakr, and J. Hong, "Technological investigation of metal 3-D printed microwave cavity filters based on different topologies and materials," *IEEE Trans. Compon., Packag., Manuf. Technol.*, vol. 12, no. 12, pp. 2027–2037, Dec. 2022.
[23] Renishaw plc. *QuantAM Build Preparation Software*. Accessed: Oct. 28, 2023. [Online]. Available: https://www.renishaw.com/en/quantam-build-preparation-software--35455
[24] T. Skaik, M. Salek, Y. Wang, M. Lancaster, T. Starke, and F. Boettcher, "180 GHz waveguide bandpass filter fabricated by 3D printing technology," in *Proc. 13th UK Europe-China Workshop Millimetre-Waves Terahertz Technol. (UCMMT)*, Aug. 2020, pp. 1–3.
[25] P. Vaitukaitis, K. Nai, J. Rao, and J. Hong, "On the development of metal 3D printed bandpass filter with wide stopband based on deformed elliptical cavity resonator with an additional plate," *IEEE Access*, vol. 10, pp. 15427–15435, 2022.
[26] H. Liu, M. Ye, Z. Ye, L. Wang, G. Wang, X. Shen, P. Xu, and C. Wang, "High-quality surface smoothening of laser powder bed fusion additive manufacturing AlSi10Mg via intermittent electrochemical polishing," *Surf. Coatings Technol.*, vol. 443, Aug. 2022, Art. no. 128608.
[27] Z.-C. Guo, G. Zhang, Y.-P. Lyu, and L. Zhu, "Multiband waveguide filters with compact size and large frequency ratio," *IEEE Trans. Plasma Sci.*, vol. 50, no. 3, pp. 761–766, Mar. 2022.

POVILAS VAITUKAITIS (Graduate Student Member, IEEE) received the M.Eng. degree (Hons.) in mechanical engineering from the University of Aberdeen, Aberdeen, U.K., in 2019. He is currently pursuing the Ph.D. degree in electrical engineering with Heriot-Watt University, Edinburgh, U.K.

His current research interests include microwave passive device design and manufacturing using metal additive manufacturing technologies.

Mr. Vaitukaitis received the Project Award for an Outstanding Master's Thesis Project from the Institution of Mechanical Engineers (IMechE), in 2019.

KENNETH NAI received the B.Sc. degree (Hons.) in electronics and electrical engineering and the Ph.D. degree in control systems from Loughborough University, Loughborough, U.K., in 1990 and 1995, respectively.

He has been with Renishaw PLC, Wotton-under-Edge, U.K., since 1995, where he is currently a Principal Engineer and has developed products in the field of metrology systems, neurosurgical robotics, and metal powder 3-D printers. He has been granted 11 U.S. patents.

Dr. Nai is a Chartered Engineer and a member of the Institution of Engineering and Technology.

JIASHENG HONG (Fellow, IEEE) received the D.Phil. degree in engineering science from the University of Oxford, Oxford, U.K., in 1994.

He then joined the University of Birmingham, Birmingham, U.K., until 2001, when he moved up to Edinburgh, U.K., to join Heriot-Watt University, Edinburgh, where he is currently a Professor in leading a team for research into advanced radio frequency (RF)/microwave device technologies. He has authored or coauthored over 200 journal articles and conference papers in this field and has published four relevant books: *Microstrip Filters for RF/Microwave Applications* (Wiley, First Edition, 2001, and Second Edition, 2011), *RF and Microwave Coupled-Line Circuits* (Artech House, Second Edition, 2007), *Balanced Microwave Filters* (Wiley, 2018), and *Advances in Planar Filters Design* (IET, 2019).

Dr. Hong is a member of the IEEE MTT Technical Committees, the Subject Editor (Microwave) of *Electronics Letters*, and an Associate Editor of *IET Microwaves, Antennas and Propagation*.